Supporting Information

Design of All-Small-Molecule Organic Solar Cells Approaching 14% Efficiency via Isometric Terminal Alkyl Chain Engineering

Haiyan Chen [1,2,3], Hua Tang [2,3], Dingqin Hu [1,2,3,*], Yiqun Xiao [4], Jiehao Fu [2], Jie Lv [2,3], Qingqing Yu [2,3], Zeyun Xiao [1,2,3], Xinhui Lu [4,*], Hanlin Hu [5,*] and Shirong Lu [1,2,3,*]

[1] Chongqing University, 174 Shazhengjie, Shapingba, Chongqing 400044, China

[2] Chongqing Institute of Green and Intelligent Technology, Chinese Academy of Sciences, Chongqing, 400714, China

[3] Chongqing School, University of Chinese Academy of Sciences, Chongqing 400714, China

[4] Department of Physics, The Chinese University of Hong Kong, Shatin, New Territories, Hong Kong, China

[5] Hoffman Institute of Advanced Materials, Shenzhen Polytechnic, 7098 Liuxian Boulevard, Shenzhen, 518055 China

[*] Correspondence: hudingqin@cigit.ac.cn (D.H.), xinhui.lu@cuhk.edu.hk (X.L.), hanlinhu@szpt.edu.cn (H.H.), lushirong@cigit.ac.cn (S.L.)

Content

1. Materials source 2

2. Material characterizations 2

3. Thin-film characterizations 2

4. Device fabrication and testing 2

5. Carrier mobility measurement 3

6. Supplementary figures 4

7. Supplementary tables 10

8. References 13

1. Materials source

All reagents and solvents for material preparation, unless otherwise specified, were purchased from Energy Chemical, Tansoole, Suna Tech, Aldrich, Sinopharm Chemical Reagent (OurChem) and JiangSu GE-Chem Biotech., Ltd. All materials for device fabrication were purchased from commercial suppliers: ITO (Youxuan Tech.), PEDOT:PSS (Clevios PVP AI. 4083 (Heraeus)), Y6 (Derthon Ltd.), Phen-NaDPO (One Material Ltd.), chloroform (Sinopharm Chemical Reagent Co., Ltd.), isopropyl alcohol (Chongqing Chuandong Chemical Co., Ltd.) and Ag (ZNXC Ltd.). All reagents and solvents were used directly without further purification.

2. Material characterizations

^{1}H-NMR and ^{13}C-NMR spectra were obtained on an AVANCE III 400 MHz nuclear magnetic resonance (NMR) spectrometer. MS was performed on an Agilent 6530 Electrospray ionization quadrupole time-of-flight mass spectrometer (ESI-Q-TOF-MS), using tetrahydrofuran as the solvent and formic acid as the assisted matrix. Cyclic voltammogram (CV) measurements were conducted on a CHI600E electrochemical workstation using a sample thin-film coated glassy carbon electrode as the working electrode, platinum (Pt) wire as the counter electrode, and Ag/AgCl as the reference electrode in a 0.1 mol L^{-1} tetrabutylammonium hexafluorophosphate (Bu_4NPF_6) acetonitrile solution. Fc/Fc^{+} redox couple was used as the inner reference for the calculation of the electronic energy levels of the donor and acceptor materials. The samples were drop-casted on the glassy carbon electrode to obtain a thin film for CV measurement. The CV curves were recorded versus the potential of standard calomel electrode (SCE), which was calibrated by the ferrocene-ferrocenium (Fc/Fc^{+}) redox couple (4.8 eV below the vacuum level). Ultraviolet−visible light (UV-vis) absorption spectra were recorded on a Perkin Elmer Lambda 365 spectrophotometer. Thermogravimetric analysis (TGA) was carried out on a METTLER TOLEDO TGA/DSC 1 thermogravimetric analyzer with thermal balance under the protection of nitrogen at a heating rate of 10 °C·min^{-1}, and differential scanning calorimetry (DSC) experiments were performed on a METTLER TOLEDO DSC 1 differential scanning calorimeter with thermal balance under the protection of nitrogen at a heating rate of 10 °C·min^{-1}.

3. Thin-film characterization

Topographic images of the films were obtained on a Bruker atomic force microscope (AFM) with the type of dimension edge with Scan Asyst™ in the tapping mode using an etched silicon cantilever at a nominal load of ~2 nN, and the scanning rate for a 10 μm × 10 μm image was 1.5 Hz. Transmission electron microscope (TEM) studies were conducted with an FEI Tecnai G2 F20 electron microscope to investigate the phase distribution of the active layer. GIWAXS measurements were carried out with a Xeuss 2.0 SAXS/WAXS laboratory beamline using a Cu X-ray source (8.05 keV, 1.54 Å) and a Pilatus3R 300K detector. The incidence angle was 0.2°. The samples for GIWAXS measurements were fabricated on silicon substrates using the same recipe for the devices.

4. Device fabrication and testing

ITO-coated glass substrates were cleaned with detergent water, deionized water, acetone, and isopropyl alcohol in an ultrasonic bath sequentially for 30 min, and further treated with UV exposure for 30 min in a UV-ozone chamber. A thin layer (ca. 30 nm) of PEDOT:PSS was first spin-coated on the substrates at 4000 rpm and baked at 120 °C for 10 min under ambient conditions. The substrates were then transferred into a nitrogen-filled glove box. The optimized concentration was 18 mg·mL^{-1}

chloroform solution with D:A ratio of 1.8:1 (w/w). After spin-coating, the blend films were treated with chloroform solvent for 30 s and annealed at 120 °C for 5 min. The active layer thickness was around 100 nm. Then, Phen-NaDPO as the electron transporting layer was spin-coated on the active layer by 2000 rpm from isopropyl alcohol solution. Finally, 100 nm of Ag electrodes was evaporated at 0.5 Å/s during the former 100 Å period and then evaporated at 2 Å s^{-1}, at a pressure of less than 2×10^{-4} Pa.

The current density–voltage (*J*–*V*) curves of OSCs were tested in air atmosphere by a Keithley 2400 source meter and an AAA grade solar simulator (Sirius-SS150A-D, Zolix Ltd.) along with AM 1.5 G spectra whose intensity was corrected by a certified standard silicon solar cell (Certificate No.: GXtc2017-1280, NIM) at 1000 $W\cdot m^{-2}$. The *J*–*V* curves were measured in the forward direction from 0.2 to 1.2 V. The external quantum efficiency (EQE) was measured by a certified incident photon to electron conversion (IPCE) equipment (QE-R) from Enli Technology Co., Ltd.

5. Carrier mobility measurement

The carrier mobility (hole and electron mobility) of the photoactive layer was obtained by fitting the dark current of hole/electron-only diodes to the space-charge-limited current (SCLC) model. Hole-only diode configuration: glass/ITO/PEDOT:PSS/active layer/MoO_3/Ag; here, V_{bi} = 0 V (flat band pattern formed by PEDOT:PSS-MoO_3). Electron-only diode configuration: glass/ITO/ZnO/Phen-NaDPO/active layer/Phen-NaDPO/Ag; here, V_{bi} = 0.5 V was used following the protocol reported [1]. The active layer thickness was determined by a Tencor surface profilometer. The electric-field-dependent SCLC mobility was estimated using the following equation [1]:

$$J(V) = \frac{9}{8}\varepsilon_0\varepsilon_r\mu_0 exp\left(0.89\beta\sqrt{\frac{V-V_{bi}}{L}}\right)\frac{(V-V_{bi})^2}{L^3}$$

6. Supplementary figures

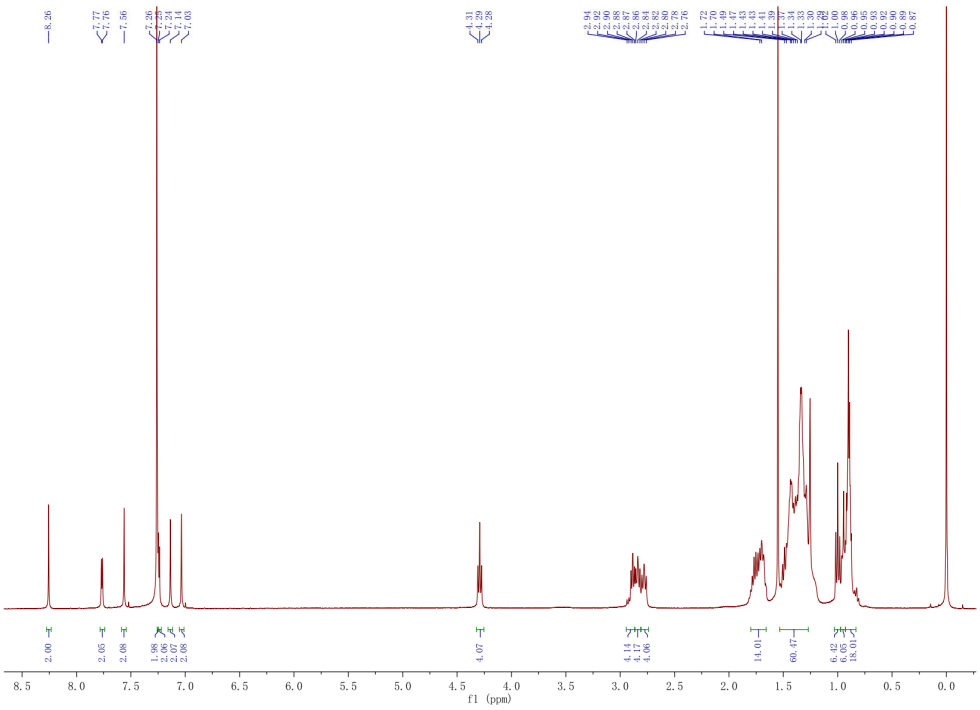

Figure S1. ^{1}H NMR spectrum of BT-Ro-Cl in $CDCl_3$.

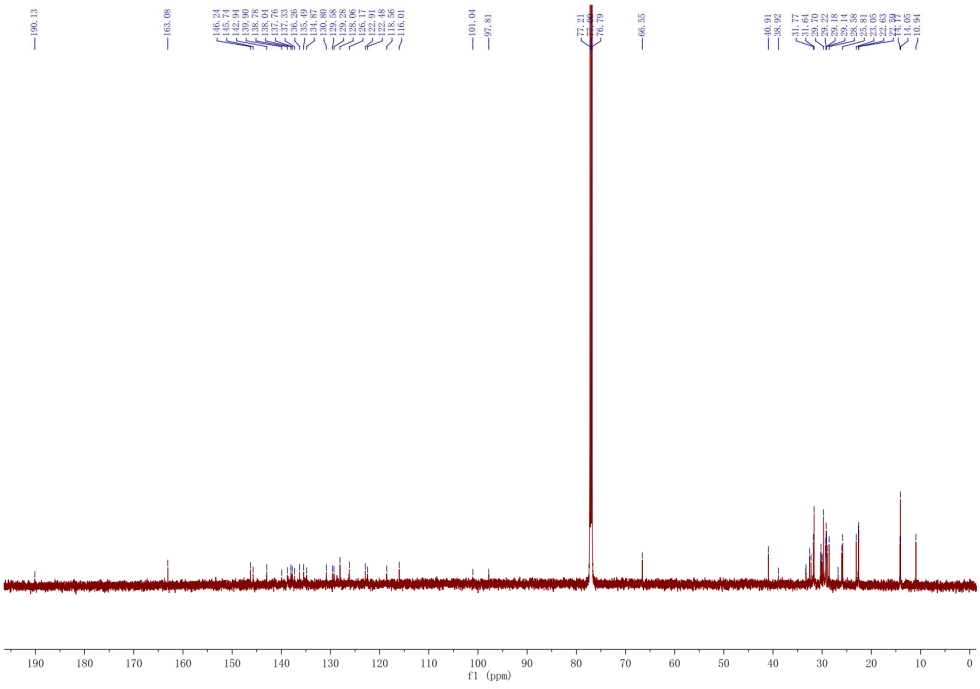

Figure S2. ^{13}C NMR spectrum of BT-Ro-Cl in $CDCl_3$.

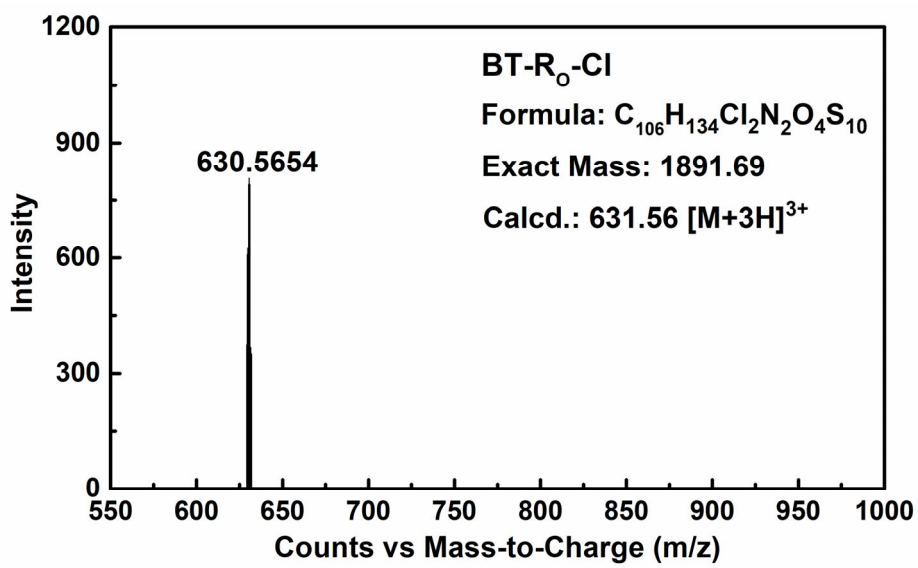

Figure S3. MS spectrum of BT-R$_O$-Cl. The formula is $C_{106}H_{134}Cl_2N_2O_4S_{10}$ with the calculated exact mass of 1891.69, and the calculated value of $[M+3H]^{3+}$ was 631.56 ($C_{106}H_{137}Cl_2N_2O_4S_{10}$). The found value of 630.57 corresponds to the m/z of $[M+3H]^{3+}$.

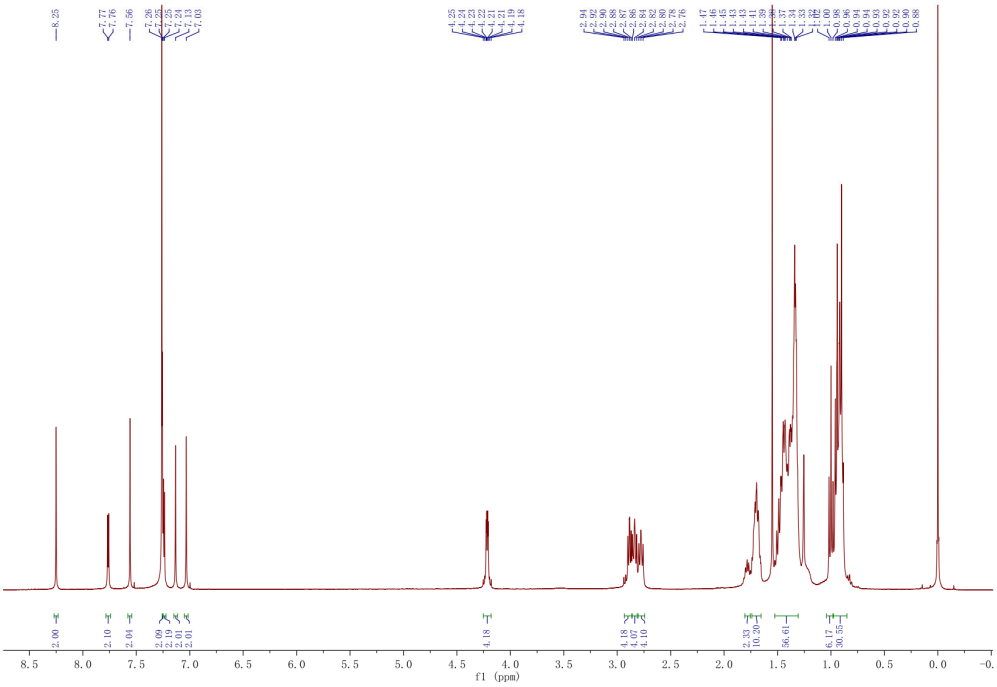

Figure S4. ^{1}H NMR spectrum of BT-R$_{EH}$-Cl in $CDCl_3$.

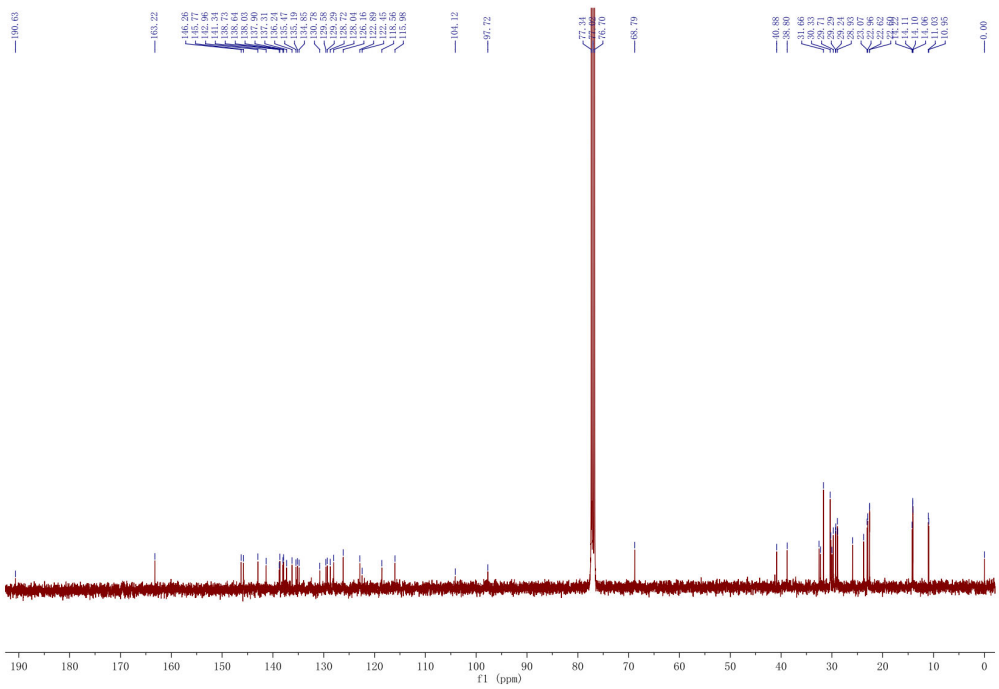

Figure S5. ^{13}C NMR spectrum of BT-R_{EH}-Cl in $CDCl_3$.

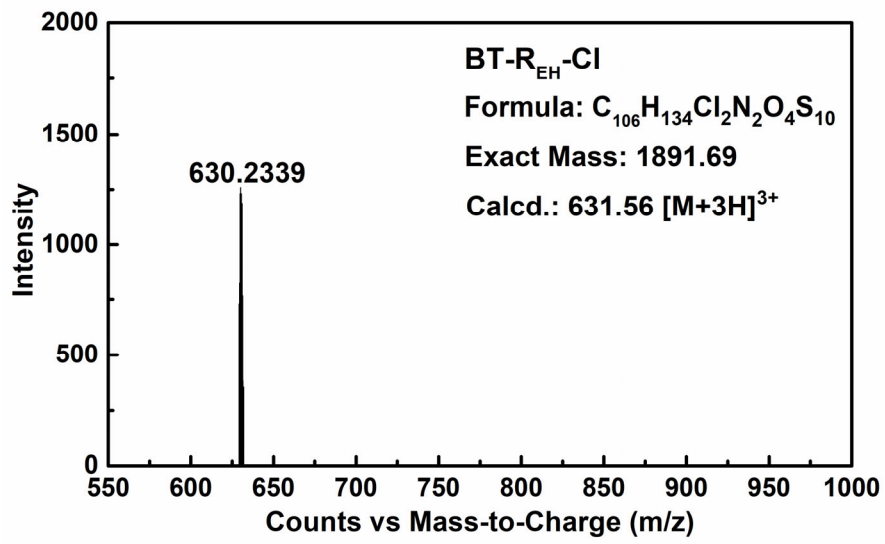

Figure S6. MS spectrum of BT-R_{EH}-Cl. The formula is $C_{106}H_{134}Cl_2N_2O_4S_{10}$ with the calculated exact mass of 1891.69, and the calculated value of $[M+3H]^{3+}$ was 631.56 ($C_{106}H_{137}Cl_2N_2O_4S_{10}$). The found value of 630.23 corresponds to the m/z of $[M+3H]^{3+}$.

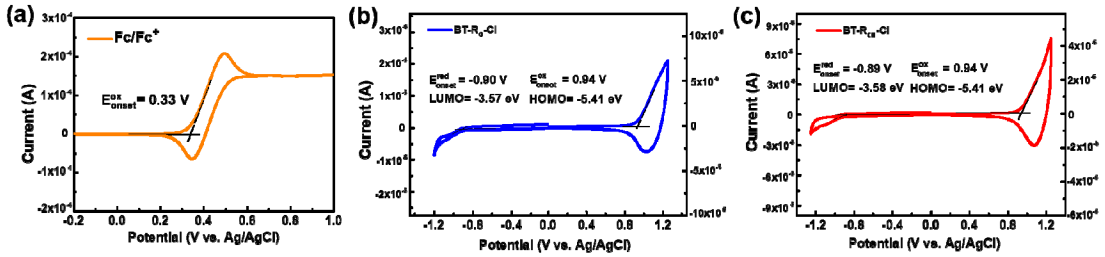

Figure S7. Cyclic voltammograms (CVs) of (a) Fc/Fc^{+}, (b) BT-Ro-Cl, and (c) BT-REH-Cl in 0.1 mol·L^{-1} tetrabutylammonium hexafluorophosphate (Bu_4NPF_6) acetonitrile solution.

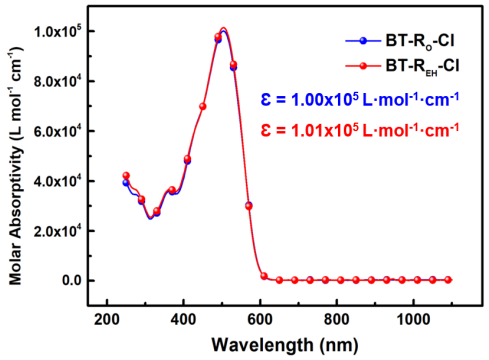

Figure S8. The molar absorption coefficient spectra of chloroform solution with both BT-Ro-Cl and BT-REH-Cl concentration of 0.01 mg·mL^{-1}.

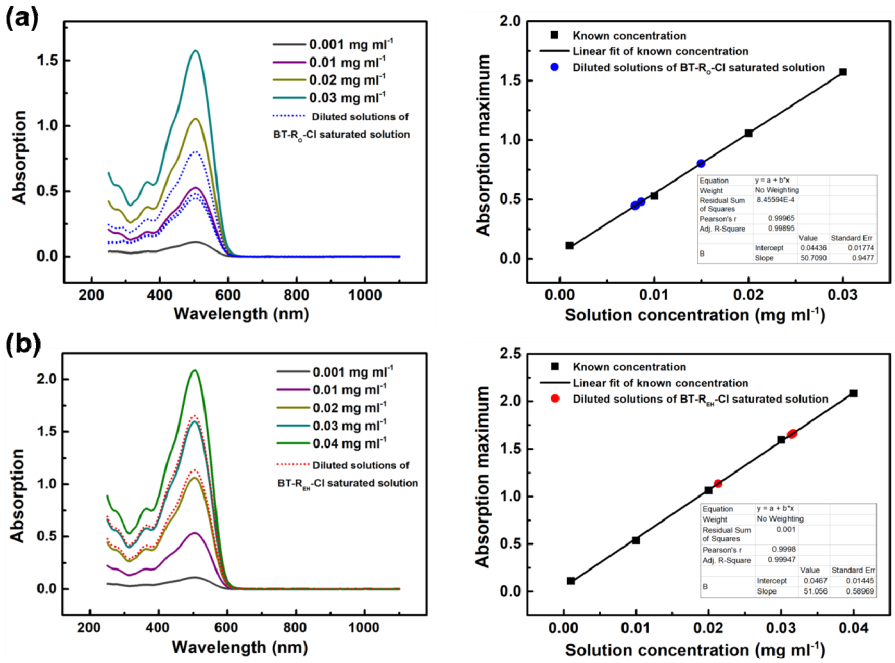

Figure S9. Derivation of the solubility of (a) BT-Ro-Cl and (b) BT-REH-Cl in chloroform. Plot of absorption maximum vs. solution concentration for donor molecules in chloroform of known concentration (black squares) and diluted solutions of donor/chloroform saturated solutions (blue dots for BT-Ro-Cl and red dots for BT-REH-Cl). The solubility of BT-Ro-Cl and BT-REH-Cl are derived

from concentration and absorption data, which are 76.5 mg mL^{-1} and 158.1 mg mL^{-1} for BT-Ro-Cl and BT-REH-Cl, respectively.

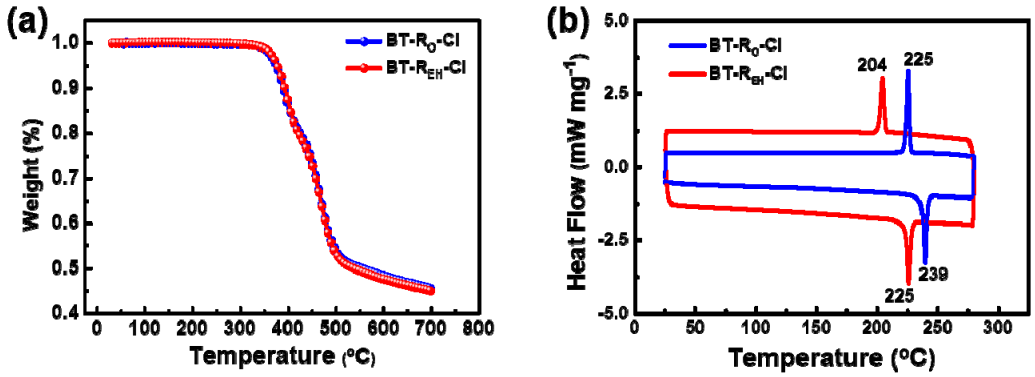

Figure S10. (a) Thermogravimetric analysis (TGA) curves and (b) differential scanning calorimetry (DSC) curves of BT-Ro-Cl and BT-REH-Cl with a heating rate of 10 °C·min $^{-1}$ under nitrogen atmosphere. The lower trace of DSC is from the second heating cycle and the upper trace from the second cooling cycle.

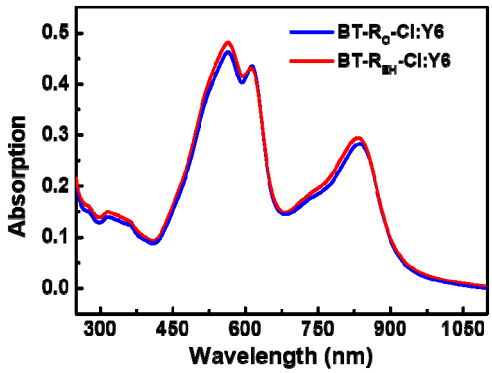

Figure S11. UV-vis absorption spectra of BT-Ro-Cl:Y6 and BT-REH-Cl:Y6 blended films. Thin-film samples were prepared under the optimal device conditions on PEDOT:PSS-coated ITO.

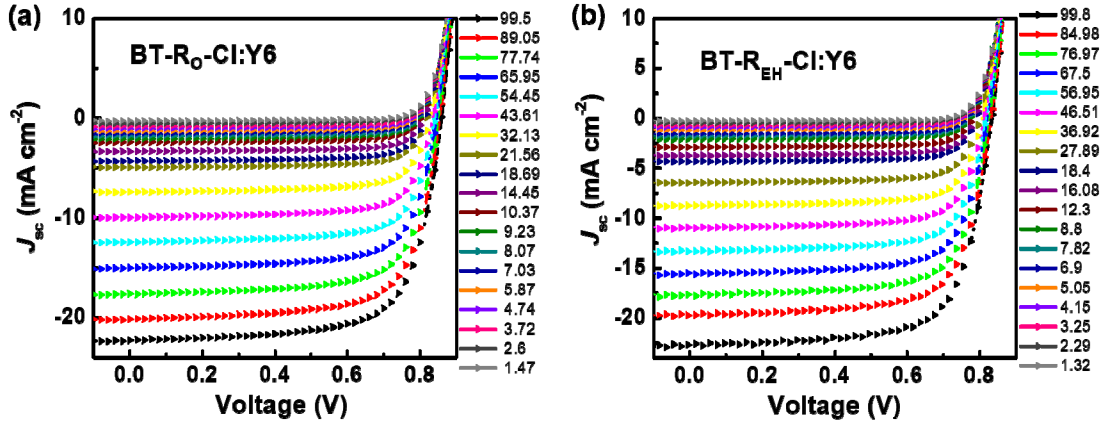

Figure S12. *J–V* curves of (a) BT-Ro-Cl:Y6 and (b) BT-REH-Cl:Y6 in various incident light intensity illuminations.

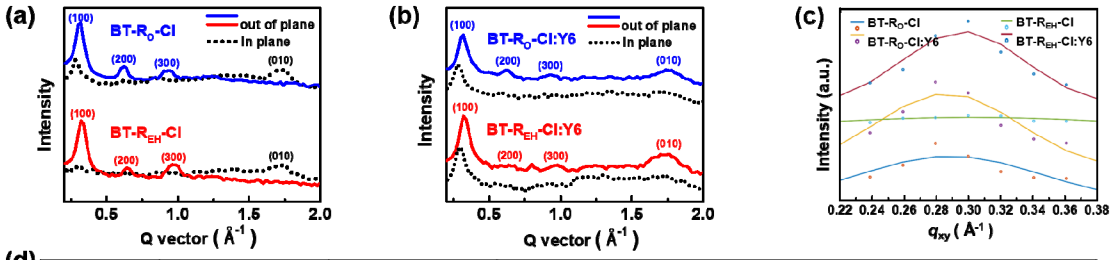

(d)

Plane	Samples	Direction and plane		π-π stacking			
				Location (Å^{-1})	D-spacing (Å)	CCL (Å)	Relative integrated intensity
In plane	BT-R$_O$-Cl	q_{xy}	(010)	1.71	3.67	13.30	
	BT-R$_{EH}$-Cl	q_{xy}	(010)	1.70	3.70	10.60	
	BT-R$_O$-Cl:Y6	q_{xy}	(010)	1.70	3.69	8.27	
	BT-R$_{EH}$-Cl:Y6	q_{xy}	(010)	1.69	3.72	7.58	
Out of plane	BT-R$_O$-Cl:Y6	q_z	(010)	1.74	3.60	12.02	1
	BT-R$_{EH}$-Cl:Y6	q_z	(010)	1.73	3.64	12.40	1.1

Plane	Samples	Direction and plane		Lamellar stacking		
				Location (Å^{-1})	D-spacing (Å)	CCL (Å)
In plane	BT-R$_O$-Cl	q_{xy}	(100)	0.29	21.70	30.80
	BT-R$_O$-Cl:Y6	q_{xy}	(100)	0.29	21.90	38.70
	BT-R$_{EH}$-Cl:Y6	q_{xy}	(100)	0.30	21.20	45.20
Out of plane	BT-R$_O$-Cl	q_z	(100)	0.31	20.20	101.00
	BT-R$_{EH}$-Cl	q_z	(100)	0.33	19.30	94.60
	BT-R$_O$-Cl:Y6	q_z	(100)	0.32	19.90	68.00
	BT-R$_{EH}$-Cl:Y6	q_z	(100)	0.33	19.20	62.80

Figure S13. (a,b) In-plane (dotted lines) and out-of-plane (solid lines) line-cut profiles of the corresponding two-dimensional GIWAXS data. (c) A part of intensity distribution and fitting curves corresponding to (100) diffractions in the q_{xy} direction. (d) The analysis data of two-dimensional GIWAXS results.

7. Supplementary tables

Table S1. Representative of highly efficient small-molecule donors using in ASM-OSCs.

Donors	Device structure	PCE/%	Ref.
BTR	ITO/PEDOT:PSS/BTR:NITI:$PC_{71}BM$/PNDIT-F3N/Al	13.63	**Error! Reference**
BTR-Cl	ITO/PEDOT:PSS/BTR-Cl:Y6/Phen-NaDPO/Ag	13.61	**Error! Reference**
	ITO/PEDOT:PSS/BTR-Cl:Y6/Phen-NaDPO/Ag	14.7	**Error! Reference**
	ITO/PEDOT:PSS/BTR-Cl:Y6:$PC_{71}BM$/Phen-NaDPO/Ag	15.34	**Error! Reference**
	ITO/PEDOT:PSS/BTR-Cl:Y6:BTP-BO-4F/PDIN/Al	14.46	[6]
	ITO/PEDOT:PSS/BTR-Cl:BTP-2F-2Cl/Phen-NaDPO/Ag	13.1	[7]
	ITO/PEDOT:PSS/BTR-Cl:BTP-FCl-FCl/Phen-NaDPO/Ag	15.3	[7]
BSFTR	ITO/PEDOT:PSS/BSFTR:Y6/ZrAcac/Al	13.69	**Error! Reference**
BTEC-2F	ITO/PEDOT:PSS/BTEC-2F:Y6/PDINO/Al	13.34	**Error! Reference**
ZR1	ITO/PEDOT:PSS/ZR1:Y6/Al	14.34	**Error! Reference**
BT-2F	ITO/PEDOT:PSS/BT-2F:Y6/PDINO/Al	13.80	**Error! Reference**
	ITO/PEDOT:PSS/BT-2F:N3/PDINO/Al	14.09	**Error! Reference**
SM1-F	ITO/PEDOT:PSS/SM1-F:Y6/PDINO/Al	14.07	**Error! Reference**
B1	ITO/PEDOT:PSS/B1:Y6/PFN-Br/Al	15.3	**Error! Reference**
BDTT-TR	ITO/PEDOT:PSS/BDTT-TR:Y6/PDINO/Al	14.03	**Error! Reference**
TBFT-TR	ITO/PEDOT:PSS/TBFT-TR:Y6-C2/PDINO/Al	13.76	**Error! Reference**

Table S2. Photovoltaic performance of BT-R_O-Cl:Y6-based devices and BT-R_{EH}-Cl:Y6-based devices without any post treatment using device architecture of ITO/PEDOT:PSS/active layer/Phen-NaDPO/Ag. The concentration of active layer was 18 mg·mL^{-1} and donor/acceptor (D/A) ratio was 1.8:1.

Active layer	V_{OC} (mV)	J_{SC} (mA·cm^{-2})	FF (%)	PCE (%)	[a] PCE (%)
BT-R_O-Cl:Y6	895.4	16.66	46.8	6.98	6.95±0.03
BT-R_{EH}-Cl:Y6	896.6	17.25	41.0	6.34	6.30±0.04

a) The average PCE values were obtained from 15 devices.

Table S3. Photovoltaic performance of BT-R_O-Cl:Y6-based devices with different donor/acceptor (D/A) ratio using device architecture of ITO/PEDOT:PSS/active layer/Phen-NaDPO/Ag, the concentration of active layer was 18 mg·mL^{-1} and annealing temperature (TA) was 120 °C for 5 min.

Device condition	V_{OC} (mV)	J_{SC} (mA·cm^{-2})	FF (%)	[a] PCE (%)
D:A = 1.0:1	842.7	22.18	57.72	10.79 (10.55 ± 0.22)
D:A = 1.4:1	840.1	22.61	61.58	11.70 (11.48 ± 0.19)
D:A = 1.6:1	834.7	22.36	64.55	12.05 (11.95 ± 0.10)
D:A = 1.8:1	839.3	22.25	65.59	12.25 (12.13 ± 0.11)
D:A = 2.0:1	838.9	22.61	64.51	12.23 (12.12 ± 0.10)

[a]The average PCE values were obtained from 15 devices.

Table S4. Photovoltaic performance of BT-Ro-Cl:Y6-based devices with different active layer thickness using the device architecture ITO/PEDOT:PSS/active layer/Phen-NaDPO/Ag, with a D/A ratio of 1.8:1 and a TA process of 120 °C for 5 min.

Thickness (nm)	V_{OC} (mV)	J_{SC} (mA·cm^{-2})	FF (%)	[a] PCE (%)
80	856.9	22.36	66.13	12.67 (12.45 ± 0.18)
100	851.6	22.92	66.73	13.03 (12.86 ± 0.16)
110	844.3	22.29	62.69	11.81 (11.48 ± 0.30)
120	841.6	21.53	60.11	10.90 (10.58 ± 0.28)
180	829.8	20.61	57.94	9.91 (9.82 ± 0.07)
300	803.4	19.85	47.42	7.56 (7.44 ± 0.11)

[a] The average PCE values were obtained from 15 devices.

Table S5. Photovoltaic performance of BT-Ro-Cl:Y6-based devices with different TA time using the device architecture ITO/PEDOT:PSS/active layer/Phen-NaDPO/Ag, active layer thickness 100 nm, and D/A ratio 1.8:1.

Device condition	V_{OC} (mV)	J_{SC} (mA·cm^{-2})	FF (%)	[a] PCE (%)
110 °C/5 min	875.2	22.37	67.76	13.26 (13.09 ± 0.15)
120 °C/5 min	865.1	22.50	68.59	13.35 (13.20 ± 0.10)
130 °C/5 min	845.1	22.40	69.63	13.18 (13.06 ± 0.12)
140 °C/5 min	838.6	22.19	69.44	12.92 (12.79 ± 0.18)

[a]The average PCE values were obtained from 15 devices.

Table S6. Photovoltaic performance of BT-Ro-Cl:Y6-based devices with different solvent vapor annealing (SVA) time of chloroform (CF) using the device architecture ITO/PEDOT:PSS/active layer/Phen-NaDPO/Ag, active layer thickness 100 nm and D/A ratio 1.8:1.

Device condition	V_{OC} (mV)	J_{SC} (mA·cm^{-2})	FF (%)	[a] PCE (%)
SVA CF/15 s	885.7	16.64	46.02	6.78 (6.65 ± 0.11)
SVA CF/20 s	858.8	22.26	60.78	11.62 (11.43 ± 0.17)
SVA CF/25 s	849.6	22.29	68.08	12.89 (12.64 ± 0.21)
SVA CF/30 s	847.3	22.51	69.32	13.22 (12.97 ± 0.20)
SVA CF/35 s	843.5	22.45	70.16	13.29 (13.11 ± 0.14)
SVA CF/40 s	841.2	22.05	69.62	12.94 (12.77 ± 0.19)

[a] The average PCE values were obtained from 15 devices.

Table S7. Photovoltaic performance of BT-REH-Cl:Y6-based devices with different donor/acceptor (D/A) ratios using the device architecture ITO/PEDOT:PSS/active layer/Phen-NaDPO/Ag, active layer concentration 18 mg·mL^{-1}, and TA process 120 °C for 5 min.

Device condition	V_{OC} (mV)	J_{SC} (mA·cm^{-2})	FF (%)	[a] PCE (%)
D:A=1.0:1	864.8	22.08	59.07	11.28 (11.20 ± 0.07)
D:A=1.4:1	861.3	22.14	61.29	11.69 (11.46 ± 0.21)
D:A=1.6:1	858.7	22.43	66.07	12.73 (12.51 ± 0.20)
D:A=1.8:1	858.4	22.72	68.95	13.45 (13.32 ± 0.13)
D:A=2.0:1	853.6	22.53	67.83	13.04 (12.89 ± 0.12)

[a]The average PCE values were obtained from 15 devices.

Table S8. Photovoltaic performance of BT-REH-Cl:Y6-based devices with different active layer thickness using the device architecture ITO/PEDOT:PSS/active layer/Phen-NaDPO/Ag, with D/A ratio 1.8:1 and TA process 120 °C for 5 min.

Thickness (nm)	V_{OC} (mV)	J_{SC} (mA·cm^{-2})	FF (%)	[a] PCE (%)
80	873.9	22.23	66.57	12.93 (12.71 ± 0.17)
100	867.3	23.07	66.66	13.34 (13.16 ± 0.15)
110	858.6	21.94	65.15	12.27 (12.10 ± 0.12)
120	854.9	21.52	63.35	11.65 (11.42 ± 0.20)
180	850.2	21.09	61.58	11.04 (11.93 ± 0.09)
300	838.1	25.09	51.70	10.87 (10.67 ± 0.16)

[a] The average PCE values were obtained from 15 devices.

Table S9. Photovoltaic performance of BT-REH-Cl:Y6-based devices with different TA times using the device architecture ITO/PEDOT:PSS/active layer/Phen-NaDPO/Ag, active layer thickness 100 nm and D/A ratio 1.8:1.

Device condition	V_{OC} (mV)	J_{SC} (mA·cm^{-2})	FF (%)	[a] PCE (%)
110 °C/5 min	875.4	22.33	67.82	13.26 (13.03 ± 0.11)
120 °C/5 min	867.6	22.93	69.86	13.90 (13.85 ± 0.06)
130 °C/5 min	854.7	22.71	70.45	13.67 (13.53 ± 0.09)
140 °C/5 min	849.7	22.34	72.11	13.69 (13.39 ± 0.21)

[a]The average PCE values were obtained from 15 devices.

Table S10. Photovoltaic performance of BT-REH-Cl:Y6-based devices with different SVA times of CF using the device architecture ITO/PEDOT:PSS/active layer/Phen-NaDPO/Ag, active layer thickness 100 nm and D/A ratio 1.8:1.

Device condition	V_{OC} (mV)	J_{SC} (mA·cm^{-2})	FF (%)	[a] PCE (%)
SVA CF/15 s	856.1	22.23	68.64	13.07 (12.91 ± 0.13)
SVA CF/20 s	854.1	22.27	70.11	13.33 (13.14 ± 0.18)
SVA CF/25 s	847.8	22.22	71.44	13.46 (13.27 ± 0.18)
SVA CF/30 s	846.0	21.98	72.08	13.28 (13.16 ± 0.10)
SVA CF/35 s	844.5	21.71	70.20	12.87 (12.71 ± 0.12)
SVA CF/40 s	832.6	21.66	69.73	12.57 (12.43 ± 0.11)

[a]The average PCE values were obtained from 15 devices.

Table S11. Summary of mobilities for BT-R$_O$-Cl:Y6- and BT-R$_{EH}$-Cl:Y6-based OSC devices.

Mobilities	μ_h (cm^2 V^{-1} s^{-1})	μ_e (cm^2 V^{-1} s^{-1})	μ_e/μ_h
BT-R$_O$-Cl:Y6	2.46×10^{-4}	2.72×10^{-4}	1.11
BT-R$_{EH}$-Cl:Y6	2.81×10^{-4}	3.01×10^{-4}	1.07

8. References

[1] Gong, Y.; Kan, Z.; Xu, W.; Wang, Y.; AlShammari, S.H.; Laquai, F.; Lai, W.-Y.; Huang, W. Wide-bandgap small molecular acceptors based on a weak electron-withdrawing moiety for efficient polymer solar cells. *Sol. RRL* **2018**, *2*, 1800120. [https://doi.org/10.1002/solr.201800120]

[2] Zhou, Z.; Xu, S.; Song, J.; Jin, Y.; Yue, Q.; Qian, Y.; Liu, F.; Zhang, F.; Zhu, X. High-efficiency small-molecule ternary solar cells with a hierarchical morphology enabled by synergizing fullerene and non-fullerene acceptors. *Nat. Energy* **2018**, *3*, 952–959. [https://doi.org/10.1038/s41560-018-0234-9]

[3] Chen, H.; Hu, D.; Yang, Q.; Gao, J.; Fu, J.; Yang, K.; He, H.; Chen, S.; Kan, Z.; Duan, T.; Yang, C.; Ouyang, J.; Xiao, Z.; Sun, K.; Lu, S. All-small-molecule organic solar cells with an ordered liquid crystalline donor. *Joule*, **2019**, *3*, 3034-3047. [https://doi.org/10.1016/j.joule.2019.09.009]

[4] Tang, H.; Chen, H.; Yan, C.; Huang, J.; Fong, P.W.K.; Lv, J.; Hu, D.; Singh, R.; Kumar, M.; Xiao, Z.; Kan, Z.; Lu, S.; Li, G. Delicate morphology control triggers 14.7% efficiency all-small-molecule organic solar cells. *Adv. Energy Mater.* **2020**, *10*, 2001076. [https://doi.org/10.1002/aenm.202001076]

[5] Hu, D.; Yang, Q.; Chen, H.; Wobben, F.; Le Corre, V.M.; Singh, R.; Liu, T.; Ma, R.; Tang, H.; Anton Koster, L.J.; Duan, T.; Yan, H.; Kan, Z.; Xiao, Z.; Lu, S. 15.34% efficiency all-small-molecule organic solar cells with improved fill factor enabled by a fullerene additive. *Energy Environ. Sci.* **2020**, *13*, 2134-2141. [https://doi.org/10.1039/d0ee00714e]

[6] Xu, C.; Chen, H.; Zhao, Z.; Gao, J.; Ma, X.; Lu, S.; Zhang, X.; Xiao, Z. ; Zhang, F. 14.46% efficiency small molecule organic photovoltaics enabled by the well trade-off between phase separation and photon harvesting. *J. Energy Chem.* **2021**, *57*, 610-617. [https://doi.org/10.1016/j.jechem.2020.09.025]

[7] Hu, D.; Yang, Q.; Zheng, Y.; Tang, H.; Chung, S.; Singh, R.; Lv, J.; Fu, J.; Kan, Z.; Qin, B.; Chen, Q.; Liao, Z.; Chen, H.; Xiao, Z.; Sun, K.; Lu, S. 15.3% Efficiency All-Small-Molecule Organic Solar Cells Achieved by a Locally Asymmetric F, Cl Disubstitution Strategy. *Adv. Sci.* **2021**, 2004262. [https://doi.org/10.1002/advs.202004262]

[8] Yue, Q.; Wu, H.; Zhou, Z.; Zhang, M.; Liu, F.; Zhu, X. 13.7% efficiency small-molecule solar cells enabled by a combination of caterial and morphology optimization. *Adv. Mater.* **2019**, *31*, 1904283. [https://doi.org/10.1002/adma.201904283]

[9] Ge, J.; Xie, L.; Peng, R.; Fanady, B.; Huang, J.; Song, W.; Yan, T.; Zhang, W.; Ge, Z. 13.34% efficiency non-fullerene all-small-molecule organic solar cells enabled by modulating the crystallinity of donors via a fluorination strategy. *Angew. Chem. Int. Ed.* **2020**, *59*, 2808-2815. [https://doi.org/10.1002/anie.201910297]

[10] Zhou, R.; Jiang, Z.; Yang, C.; Yu, J.; Feng, J.; Abdullah Adil, M.; Deng, D.; Zou, W.; Zhang, J.; Lu, K.; Ma, W.; Gao, F.; Wei, Z. All-small-molecule organic solar cells with over 14% efficiency by

optimizing hierarchical morphologies. *Nat. Commun.* **2019**, *10*, 5393 [https://doi.org/10.1038/s41467-019-13292-1]

[11] Gao, J.; Ge, J.; Peng, R.; Liu, C.; Cao, L.; Zhang, D.; Fanady, B.; Hong, L.; Zhou, E.; Ge, Z. Over 14% efficiency nonfullerene all-small-molecule organic solar cells enabled by improving the ordering of molecular donor via side-chains engineering. *J. Mater. Chem. A* **2020**, *8*, 7405-7411. [https://doi.org/10.1039/d0ta01893g]

[12] Qiu, B.; Chen, Z.; Qin, S.; Yao, J.; Huang, W.; Meng, L.; Zhu, H.; Yang, Y.M.; Zhang, Z.-G.; Li, Y. Highly efficient all-small-molecule organic solar cells with appropriate active layer morphology by side chain engineering of donor molecules and thermal annealing. *Adv. Mater.* **2020**, *32*, 1908373. [https://doi.org/10.1002/adma.201908373]

[13] Qin, J.; An, C.; Zhang, J.; Ma, K.; Yang, Y.; Zhang, T.; Li, S.; Xian, K.; Cui, Y.; Tang, Y.; Ma, W.; Yao, H.; Zhang, S.; Xu, B.; He, C.; Hou, J. 15.3% efficiency all-small-molecule organic solar cells enabled by symmetric phenyl substitution. *Sci. China Mater.* **2020**, *63*, 1142–1150. [https://doi.org/10.1007/s40843-020-1269-9]

[14] Sun, R.; Wu, Y.; Guo, J.; Luo, Z.; Yang, C.; Min, J. High-efficiency all-small-molecule organic solar cells based on an organic molecule donor with an asymmetric thieno[2,3-f]benzofuran unit. *Sci. China Chem.* **2020**, *63*, 1246–1255. [https://doi.org/10.1007/s11426-020-9753-x]